

A Gapped Phase in Semimetallic T_d -WTe₂ Induced by Lithium Intercalation

Mengjing Wang^{1,2}, Aakash Kumar^{1,2}, Hao Dong^{2,3}, John M. Woods^{1,2}, Joshua V. Pondick^{1,2},
Shiyu Xu^{1,2}, Peijun Guo^{2,3}, Diana Y. Qiu^{1,2}, Judy J. Cha^{1,2*}

¹ Department of Mechanical Engineering and Materials Science, Yale University, New Haven, CT 06511, USA.

² Energy Sciences Institute, Yale West Campus, West Haven, CT 06516, USA.

³ Department of Chemical and Environmental Engineering, Yale University, New Haven, CT 06511, USA.

* judy.cha@yale.edu

Abstract

The Weyl semimetal WTe₂ has shown several correlated electronic behaviors, such as the quantum spin Hall effect, superconductivity, ferroelectricity, and a possible exciton insulator state, all of which can be tuned by various physical and chemical approaches. Here, we discover a new electronic phase in WTe₂ induced by lithium intercalation. The new phase exhibits an increasing resistivity with decreasing temperature and its carrier density is almost two orders of magnitude lower than the carrier density of the semi-metallic T_d phase, probed by *in situ* Hall measurements as a function of lithium intercalation. Our theoretical calculations predict the new lithiated phase to be a charge density wave (CDW) phase with a bandgap of ~ 0.14 eV, in good

agreement with the *in situ* transport data. The new phase is structurally distinct from the initial T_d phase, characterized by polarization angle-dependent Raman spectroscopy, and large lattice distortions close to 6 % are predicted in the new phase. Thus, we report the first experimental evidence of CDW in T_d -WTe₂, projecting WTe₂ as a new playground for studying the interplay between CDW and superconductivity. Our finding of a new gapped phase in a two-dimensional (2D) semi-metal also demonstrates electrochemical intercalation as a powerful tuning knob for modulating electron density and phase stability in 2D materials.

Main

Two-dimensional (2D) orthorhombic tungsten ditelluride (T_d -WTe₂) is a type-II Weyl semimetal in bulk and a topological insulator as a monolayer, stimulating studies of quantum electronic phases and search for topological superconductivity¹⁻⁴. Superconductivity with T_c of 580 mK has been realized in monolayer T_d -WTe₂ by electrostatic doping at an electron density of 5×10^{12} e/cm²^{1,2}, and T_c was raised to ~ 2.6 K by chemical intercalation of potassium in bulk T_d -WTe₂ where the potassium is expected to donate charge to WTe₂⁵. With electron doping, a charge density wave (CDW) may emerge in WTe₂ as several 2D chalcogenides, such as TaS₂, possess superconductivity as well as CDWs that are modulated by electron density⁶⁻⁹. Recent theoretical papers indeed predict that a high level of electron doping of over 10^{14} e/cm² in monolayer T_d -WTe₂ can introduce lattice distortions and form a CDW phase¹⁰⁻¹², neighboring the superconducting dome at 10^{13} e/cm². However, no experimental reports of a CDW phase in WTe₂ are found in the literature.

Here, we use lithium intercalation to modulate the carrier density of WTe_2 beyond the charge doping range achievable by ionic liquid gating and discover a new electronic phase in WTe_2 , which we identify as a CDW phase. With controllable lithium intercalation and deintercalation, we observe a reversible structural and electronic phase transition as evidenced by *in situ* optical, Raman, and electrical transport characterization throughout the intercalation. Structurally, the new phase shows distinct Raman peaks with crystal symmetry different from the T_d symmetry, in agreement with the T_d' phase recently reported by Muscher *et al*¹³. Electronically, despite the significant electron doping by lithium, the new phase exhibits a reduction of electron carrier density by almost two orders of magnitude compared to the pristine semi-metallic WTe_2 and increasing resistance with decreasing temperature, suggesting a bandgap opening. Our *ab initio* band structure computed within density functional theory (DFT) shows that the lithiated T_d' phase develops an indirect bandgap of 0.14 eV and a direct bandgap of 0.66 eV, consistent with the experimentally observed semiconductor-like electrical behavior. Furthermore, calculations of the phonon dispersion reveal that the T_d phase exhibits a phonon softening with lithium intercalation at the level of the experimental phase transition and at wave vectors roughly consistent with the formation of a 2×2 folding of the Brillouin zone. Concomitantly, lithiation stabilizes the T_d' phase, which is a 2×2 superlattice of the T_d phase involving a distortion of the W chain along a -axis where the W-Te-W bond lengths are shortened and elongated in their successive arrangements in contrast to the identical W-Te-W bond lengths in the T_d phase. Overall, the a and c lattice parameters are strained by 4.9 % and 5.84 % respectively when WTe_2 changes from the T_d to the T_d' phase. Thus, we report the first experimental evidence of a gapped CDW phase in WTe_2 enabled by lithium intercalation.

Lithium intercalation induced phase transition

For lithium intercalation, we construct a WTe₂ flake electrochemical cell using liquid or polymer gel electrolyte with capabilities of *in situ* Raman and *in situ* transport measurements (**Figure 1a**, Methods). The exfoliated WTe₂ flakes have a lateral size distribution of 20 ~ 50 μm and a thickness range of 30 ~ 100 nm (> 50 layers) (**Figure S1**, Supplementary Information). By controlling the electrochemical intercalation voltage (V_{EC}) between the WTe₂ flake (cathode) and lithium metal (anode), lithium ions can be controllably inserted into the van der Waals gaps of the WTe₂ flake (**Figure 1b**). Lower values of V_{EC} represent more lithium ions intercalated into WTe₂ flakes.

A new structural phase emerges with distinct Raman modes at V_{EC} of 0.8 V vs Li⁺/Li in a polymer cell (**Figure 1c, d**, **Figure S2**, Supplementary Information) or at V_{EC} of 1.2 V vs Li⁺/Li in a liquid cell (**Figure S3**, Supplementary Information). In the low frequency region (< 50 cm⁻¹) of the Raman spectrum where inter-layer vibration modes are active, the shear mode of the T_d phase at ~ 8 cm⁻¹¹⁴ splits into two peaks at 6 cm⁻¹ and 13 cm⁻¹, as illustrated in **Figure 1c**. In the high frequency region (> 50 cm⁻¹) where intralayer phonon modes are populated, several Raman modes with distinct peak positions appear (**Figure 1d**). These new Raman peaks do not match those observed in the initial T_d, 1T' or 2H of WTe₂ (**Table S1**, Supplementary Information). The Raman spectrum of the new phase has two key characteristics: increased number of Raman active modes compared to the T_d phase and no discernible patterns in the peak shifts of the Raman modes relative to the T_d phase. Therefore, the new Raman modes are not a result of strain or electron doping, but a manifestation of phase transition to a new phase with atomic configurations distinct from the T_d phase. Recently, Muscher *et al.* reported a new lithiated T_d'-

WTe₂ phase whose Raman modes match our experimental data¹³ (**Table S1**, Supplementary Information). Therefore, we identify the new lithiated phase in this work to be the same as that reported by Muscher *et al.* and henceforth refer to it as the lithiated T_d' phase (T_d' when referring to the structure without any Li atoms). Optically, when WTe₂ is in the lithiated T_d' phase, dark streaks appear along the crystallographic axis *b*, perpendicular to the direction of the W-W chain, as depicted in the inset of **Figure 1c**. A closer scrutinization of the streaks *via* scanning electron microscopy (**Figure S4**, Supplementary Information) indicates them to be wrinkles, suggesting the cause of the dark streaks to be an anisotropic strain induced during the phase transition from T_d to T_d'.

A representative evolution of the high frequency Raman peaks as V_{EC} is lowered from open circuit voltage (OCV) to 0.4 V *vs* Li⁺/Li in a polymer cell is shown in **Figure 2b** with corresponding optical images in **Figure 2a**. Three distinct stages take place in the course of lithium intercalation. First, WTe₂ remains in T_d phase when $OCV > V_{EC} > 0.8V$ *vs* Li⁺/Li with negligible changes in the Raman spectra and the optical contrast. In the second stage, when $0.8 V > V_{EC} > 0.4 V$ *vs* Li⁺/Li, WTe₂ is in the new lithiated T_d' phase characterized by the distinct Raman modes and dark streaks appearing along the *b* axis (**Figure 2a**). Lastly, when $V_{EC} < 0.4 V$ *vs* Li⁺/Li, WTe₂ becomes amorphous, supported by the featureless Raman spectrum and a yellowish hue color change in WTe₂.

The resistance of the WTe₂ flake undergoing the phase transition was simultaneously tracked by two terminal measurements of the same device (**Figure 2c**). First, the resistance does not change much while WTe₂ remains in the T_d phase (grey shaded region). While V_{EC} is at 0.8 V *vs* Li⁺/Li,

the resistance starts to increase from 386 Ω at ~ 2000 s to 1015 Ω at ~ 3000 s. This resistance increase is surprising as lithium intercalation in transition metal dichalcogenides (such as MoS₂) generally leads to a decreased resistivity¹⁵ due to the extra electrons donated by Li. When WTe₂ is in the lithiated T_d' phase with the distinct Raman modes ($V_{EC} = 0.8$ V vs Li⁺/Li between 3000 s to 10000 s, pink shaded region), the resistance continues to increase and eventually saturates at 7032 Ω , a nearly twenty times increase in resistance from the pristine T_d phase. The saturated resistance indicates a completion of the phase transition. At V_{EC} of 0.4 vs Li⁺/Li, WTe₂ starts to break down and becomes amorphous, accompanied with an irreversible sharp increase in resistance (purple shaded region).

For further characterization of the crystal structure and the electronic band structure of the lithiated T_d' phase, we performed *in situ* angle-resolved Raman spectroscopy and *in situ* magneto-transport measurements, which we discuss in the following sections.

***In situ* angle-resolved Raman spectroscopy of the lithiated T_d' phase**

To characterize the crystal symmetry of the new phase, we performed *in situ* angle-resolved Raman spectroscopy, as presented in **Figure 3** (full spectra in **Figure S5**, Supplementary Information). As a function of the angle θ between the polarization direction of the incident laser and the vertical dashed line shown in **Figure 3a**, we acquired the angle dependent Raman spectra of the pristine T_d phase (**Figure 3b**) and the lithiated T_d' phase (**Figure 3e**). The lithiated T_d' phase has more Raman active modes, albeit with weaker intensities, than T_d in the range from 50 to 220 cm⁻¹, suggesting a lower crystal symmetry of the T_d' phase. Additionally, the symmetry of the prominent Raman modes is two-fold in the lithiated T_d' phase, such as the peaks centered

at 80 and 210 cm^{-1} , while the symmetry of the Raman modes is mostly four-fold in the T_d phase, e.g., peaks at 75, 130, and 214 cm^{-1} . The pole graphs of the Raman modes near 210 cm^{-1} clearly show the four-lobed and two-lobed nature of the Raman modes in T_d and lithiated T_d' phase, respectively (**Figure 3c** and **Figure 3f**).

***In situ* magneto-transport measurements during lithium intercalation**

The twenty-fold resistance increase of WTe_2 from the initial T_d phase to the lithiated T_d' phase suggests there may be a significant change in the electronic band structure of WTe_2 in the new T_d' phase. To answer this, we carried out *in situ* magneto-transport measurements of a WTe_2 flake as a function of Li intercalation.

Prior to intercalation, magneto-transport of a pristine WTe_2 flake was measured at 2 K, which showed clear Shubnikov-de Hass oscillations in high magnetic fields (**Figure S6**, Supplementary Information), suggesting a high crystal quality of WTe_2 . Fitting the R_{xx} and R_{xy} to a two-band transport model^{16, 17} showed that the pristine WTe_2 flake has an almost equally compensated electron and hole density at 2 K ($n_e = 2.11 \times 10^{20} \text{ cm}^{-3}$; $n_h = 1.97 \times 10^{20} \text{ cm}^{-3}$; **Figure S6**, Supplementary Information). The nearly balanced electron and hole population indicates that the Fermi level (E_F) is close to zero in pristine WTe_2 intersecting the conduction band and valence band equally at 2 K, as predicted by DFT¹⁶ and visualized in **Figure 4a**. At 300 K, transport data of the pristine WTe_2 flake suggests that electrons are populated more than holes (**Figure S7 f-g**, Supplementary Information) and thereby conduction is primarily carried out by electrons at room temperature.

During intercalation, both R_{xx} and R_{xy} were measured in the magnetic field of 3 T at 300 K as V_{EC} was swept from OCV to 0.8 V, as displayed in **Figure 4c-d**. In accordance with the Raman observation that new Raman modes from T_d' emerge when V_{EC} stays at 0.8 V for 30 mins, a red vertical line in **Figure 4c-d** marks the phase transition point from T_d to lithiated T_d' phase. When WTe_2 stays in T_d during $OCV > V_{EC} > 0.8 \text{ V vs Li}^+/\text{Li}$, R_{xx} remains almost unchanged and decreases marginally at 1.0 V vs Li^+/Li from 32 Ω to 28 Ω , likely due to electron doping from Li. At V_{EC} of 0.8 V vs Li^+/Li , R_{xx} rises immediately and saturates at 2620 Ω after 50 mins at 0.8 V vs Li^+/Li , indicating a completion of phase transition from T_d to lithiated T_d' phase. The increase of R_{xx} measured with four probes agrees with the two-terminal measurement shown in **Figure 2c**.

Unlike the steady increase of R_{xx} at $V_{EC} = 0.8 \text{ V vs Li}^+/\text{Li}$, the Hall resistance R_{xy} shows a plateau that lasts about 30 mins before it starts to increase. According to the *in situ* Raman data, WTe_2 stays as T_d phase during the first 30 mins at $V_{EC} = 0.8 \text{ V}$. Therefore, the plateau region of R_{xy} suggests a potential intermediate WTe_2 phase, which does not have drastic lattice rearrangements that can be detected by Raman spectroscopy but possesses a distinct electron band structure from that of T_d . After the plateau, R_{xy} increases and eventually saturates at 45 Ω in the new T_d' phase. After removing the contribution from R_{xx} due to the imperfect alignment of the Hall electrodes (see Methods), the plateau region persists in the corrected R_{xy} , but the sign changes from positive to negative in the new T_d' phase, suggesting a hole-dominated transport (**Figure S8**, Supplementary Information). **Figure 4e** shows the Hall carrier density (n_{Hall}) determined from the corrected R_{xy} . When $OCV > V_{EC} > 0.8 \text{ V vs Li}^+/\text{Li}$, n_{Hall} remains unchanged at $7.6 \times 10^{15} \text{ cm}^{-2}$ as WTe_2 is in the T_d phase. The spikes seen in n_{Hall} correspond to the regions where the differences of R_{xy} values between 3 T and 0 T are very small, and therefore are artifacts and not

physically meaningful. At the onset of $V_{EC} = 0.8$ V, n_{Hall} falls considerably to 9.1×10^{14} cm⁻² and remains at this density. After ~ 30 mins at $V_{EC} = 0.8$ V, WTe₂ is in the lithiated T_d' phase and n_{Hall} changes the sign with a further reduced hole carrier density of 1.9×10^{14} cm⁻².

The observed characteristics of R_{xx} and R_{xy} are reproduced in the second round of lithium intercalation (**Figure S7 a-c**, Supplementary Information) and in a different Hall bar device (**Figure S9**, Supplementary Information), confirming the reversibility of the phase transition and ruling out the possibilities of electrical contact degradation for the observation. We also confirm that the electrical contacts remain unaffected by intercalation as the magneto-transport behaviors remain unchanged between pristine state and deintercalated state (**Figure S7 f-g**, Supplementary Information). Therefore, the increase of resistance and accompanying reduction of carrier density exclusively originate from the change in the electronic band structure as WTe₂ changes to the new lithiated T_d' phase from T_d.

The reduced carrier density and the change of the carrier type suggests a potential gap opening in initially semimetallic WTe₂. To test this hypothesis, temperature-dependent R_{xx} were acquired at pristine state (**Figure S10**, Supplementary Information) as well as at various stages of intercalation by first halting the intercalation through rapid quenching to 200 K, as shown in **Figure 4b**. At $OCV > V_{EC} > 0.8$ V vs Li⁺/Li, lithiated WTe₂ remains in the T_d phase and R_{xx} vs T curves show a metallic transport with decreasing resistance at lower temperatures. In contrast, at $V_{EC} \leq 0.8$ V vs Li⁺/Li, the lithiated WTe₂ behaves like a semiconductor with resistance increasing with decreasing temperature. This suggests that the new lithiated T_d' phase has a bandgap, in contrast to the starting semimetallic T_d phase, as illustrated in **Figure 4a**. We note that the

temperature range was limited to 150 K for transport measurements due to the sudden volume change of the polymer electrolyte at that temperature, which breaks the devices.

We carried out DFT calculations of the electronic band structure of the T_d and T_d' phases (**Figure 5a-b**) to elucidate the origin of the dramatic differences in the electron transport of these phases.

The lithiated T_d' phase has a simple monoclinic¹³ conventional unit cell with twice the number of atoms of the orthorhombic T_d unit cell, as illustrated in **Figure 5a-b**. Detailed crystallographic information of T_d and lithiated T_d' is summarized in **Table S2** and **Table S3**, Supplementary Information. The computed band structure for pristine T_d phase in **Figure 5c** shows that the electron pocket is slightly larger than the hole pocket, consistent with our magneto-transport data of pristine T_d state. Moreover, the band structure of the lithiated T_d' phase in **Figure 5d** confirms that there is a gap opening in the lithiated T_d' phase with a direct gap of 0.66 eV and an indirect gap of 0.14 eV along the Γ -X direction. The proximity of the Fermi level to the valence band maximum further suggests a hole-dominant transport behavior in lithiated T_d' phase, which confirms the finding of electron to hole transport transition in our *in situ* magneto-transport measurements.

Mechanism of the phase transition and formation of CDWs

The crystal structure of the lithiated T_d' phase was recently discovered using single crystal X-ray crystallography by Muscher *et al*¹³. Remarkably, the same crystal structure was theoretically predicted to be a 2×2 CDW in monolayer WTe_2 under electron doping at a level of 0.5 electrons per unit cell ($9.04 \times 10^{13} \text{ e/cm}^2$)^{10, 11}. This strongly suggests that the new phase we observe

coincides with the predicted 2×2 CDW and that the CDW formation is driven by the extremely high levels of electron doping from Li intercalants.

To confirm the CDW nature of the new phase in bulk and explore the mechanism driving the phase transition, we computed the phonon dispersion of the lithiated T_d phase in bulk as shown in **Figure 6**. Our Bader charge¹⁸ analysis suggests that each Li atom dopes ~ 0.85 e to the Te atoms. Accordingly, we computed the phonon dispersion of the lithiated T_d phase for two concentrations of electronic doping: 1 Li atom/unit cell ($T_d\text{-Li}_{0.25}\text{WTe}_2$) in **Figure 6b** and implicit doping at a concentration equivalent to the level of doping by Li in the lithiated T_d' phase ($T_d'\text{-Li}_{0.5}\text{WTe}_2$) in **Figure S11**, Supplementary Information. The phonon dispersion of the pristine T_d phase in **Figure 6a** shows a stable structure. Upon introduction of 1 Li atom per unit cell, the phonon branch along the X-S-Y path in the Brillouin zone becomes soft, suggesting the instability of the lattice and the possible formation of a CDW, similar to the picture of the CDW phase diagram predicted in monolayer WTe_2 ¹⁰. A similar softening is also observed in the case of the implicitly doped T_d in **Figure S11**, Supplementary Information, indicating that high level of electron doping alone leads to lattice instability. On the contrary, the lithiated T_d' phase ($T_d'\text{-Li}_{0.5}\text{WTe}_2$) shows a stable phonon dispersion in **Figure 6c** while the removal of Li atoms in the T_d' phase softens the phonon modes along the X-H₁-C-H-Y path in **Figure 6d**. Energetically, the phase transition from T_d to the T_d' is driven by the greater negative formation energy of T_d' (2×2 CDW) than the lithiated $T_d\text{-WTe}_2$ at the same Li concentration. Based on our DFT calculations, the change in enthalpy in going from $T_d\text{-WTe}_2$ to lithiated $T_d'\text{-Li}_{0.5}\text{WTe}_2$ is -0.62 eV, whereas it is -0.36 eV going from T_d to lithiated $T_d\text{-Li}_{0.5}\text{WTe}_2$.

Conclusion

A new gapped phase is discovered in semi-metallic T_d - WTe_2 , stabilized by an exceptionally high level of electron doping from lithium intercalation. We identified the structure of the new phase to be a lithiated T_d' phase by *in situ* angle-resolved Raman spectroscopy. A bandgap opening in the new phase is suggested by *in situ* transport measurements that show an increasing resistance with decreasing temperature and a much-reduced carrier density. Our DFT calculations show that this new lithiated T_d' phase has an indirect gap of 0.14 eV and a direct bandgap of 0.66 eV. Furthermore, the structure of the lithiated T_d' phase is identical to the unit cell of the predicted 2×2 CDW in WTe_2 monolayer by electron doping¹⁰, and phonon dispersion calculations show that lithiation induces phonon softening in the T_d phase at various electron doping levels. Therefore, we identify this new lithiated T_d' phase to be a 2×2 CDW in WTe_2 , landing at the high electron doping end in the electronic phase diagram of WTe_2 , past the superconductivity phase of WTe_2 ¹¹.

Our discovery of the CDW phase in type II Weyl semimetal WTe_2 not only enriches the phase diagram of WTe_2 , but also renders WTe_2 a versatile material platform to study the interplay between superconductivity and CDW. We envision that the exceptional electron doping using lithium intercalation can also introduce CDW in other 2D transition metal dichalcogenide systems that are not known to host CDW in their intrinsic state, such as $1T'$ - $MoTe_2$. Thus, the greatly expanded electronic and structural phase diagram of 2D materials accessible using lithium intercalation will stimulate the research for novel quantum phases, such as topological superconductivity. Additionally, the sharp switch of electrical resistance of layered WTe_2 by controllable tuning of electrochemical intercalation voltage projects prospective applications in resistive memory.

Acknowledgements

M. W. and J. J. C. gratefully acknowledge the support from the Moore Foundation under the EPIQS Synthesis Investigator Award program. The electrochemical cell was developed with the support from the NSF CAREER 1749742. We also gratefully acknowledge discussions with Dr. Evan Reed, Dr. Aaron Lindenberg, Dr. Jun-Ho Lee, and Dr. Young-Woo Son. D.Y.Q. and A.K. were supported by the U.S. Department of Energy (DOE), Office of Science, Office of Basic Energy Sciences Early Career Research Program under Award Number DE-SC0021965. The calculations used resources of the National Energy Research Scientific Computing (NERSC), a DOE Office of Science User Facility operated under contract no. DE-AC02-05CH11231; the Extreme Science and Engineering Discovery Environment (XSEDE), which is supported by National Science Foundation grant number ACI-1548562; and the Oak Ridge Leadership Computing Facility at the Oak Ridge National Laboratory, which is supported by the Office of Science of the U.S. DOE under Contract No. DE-AC05-00OR22725. We also thank the Yale Center for Research Computing for the calculations carried out on the Grace supercomputer.

Methods

Device Fabrication

The WTe₂ flakes were mechanically exfoliated from the bulk WTe₂ crystals purchased from 2D Semiconductors. WTe₂ flakes with desired lateral size and thickness were wet transferred onto SiO₂/Si wafer with the assistance of KOH¹⁹. The thickness of the flake was determined by Cypher ES atomic force microscope from Asylum Research. For the device fabrication,

electrodes were written by electron beam lithography (Nabity NPGS, Helios G4 FIB-SEM) at a voltage of 30 kV and a current of 1.6 nA with a dose of 410 $\mu\text{C}/\text{cm}^2$. The developed devices were deposited with 15 nm Cr and 200 nm Au using a thermal evaporator (MBraun EcoVap) at a pressure of 10^{-7} mbar. The devices were transferred into an argon glovebox with an O_2 and H_2O level below 1 ppm right after the liftoff to minimize the oxidation.

Electrochemical Intercalation Cell Fabrication

All the intercalation cells discussed in the main text adopted a planar cell configuration with both WTe_2 electrode and lithium electrode on a piece of transparent glass slide or SiO_2/Si wafer. The detailed fabrication steps are described in our previous research papers^{19, 20}. For the liquid cells, the liquid electrolyte of 1 M LiPF_6 (EC/DEC, v:v= 50:50, battery-grade, Sigma-Aldrich) was injected into the cell to submerge the lithium and the device. For polymer cells, 0.227 g 1 M LiPF_6 solution was premixed with 0.475 g PEGMA and 1.145 g BEMA in a tarnished glass vial stirred overnight inside the glovebox. Then, 46 mg of photo-initiator was added to the well-mixed electrolyte and stirred for an additional hour in dark prior to the actual use. The mixed polymer electrolyte was drop-cast onto the target device using a micro-pipette covering both Li/copper foil and the WTe_2 device, then cured under UV light for 10 mins to form a gel-like electrolyte. The assembled intercalation cells have a cover slip with an air-tight seal that protects the cell from air and moisture.

In situ Raman Characterization

The assembled cell was taken out from the glovebox and quickly mounted to the Raman sample stage within 10 mins. Intercalation of lithium ions was driven by applying voltage between the Li

and WTe₂ electrode potentiostatically with a Biological SP300 potentiostat/galvanostat. *In situ* Raman spectra were collected during lithium intercalation using a Horiba LabRAM HR Evolution Spectrometer (grating: 1800 lines/mm) with an excitation wavelength of 633 nm at 10% power (3.5 mW).

In situ Low Frequency Raman and Angle-Resolved Raman Measurement

The low frequency and angle dependent Raman spectra were acquired using a frequency-stabilized 785 nm laser (Toptica) as the excitation source with an incident power adjusted to 5.6 mW by a neutral-density filter. A set of five narrow-linewidth, reflective volume Bragg grating notch filters (OptiGrate) was used to reject the laser and allow for measurements of Raman signals down to about 5 cm⁻¹. The polarization of the incident beam was controlled by a zero-order half-waveplate, and the polarization of scattered Raman signal was first set by a broadband linear polarizer, and then rotated by a broadband half waveplate to maintain a fixed polarization of the Raman light sent into the spectrometer. The Raman signal was spatially filtered by a pair of 75-mm focal-length achromatic lens and a 50- μ m pinhole, before sent into the spectrograph (Andor Kymera 328i) and captured by a Si EMCCD (Andor iXon Life 888). A super-long-working distance objective lens (10X, NA=0.28) was used in the measurements.

In situ Two Terminal Electrical Transport Measurement

In situ two terminal electrical transport data were collected using a semiconductor device analyzer (Agilent Technologies B1500A) during the potentiostatic lithium intercalation. The drain-source voltage applied was 50 mV, and the resistance was extracted from the slope of the *I-V* curve using a linear regression method.

Low Temperature Magneto-Transport Measurement

Magneto-transport measurements of pristine T_d-WTe₂ at 2 K were carried out with Quantum Design's DynaCool PPMS system at AC mode (17.777 Hz). The system was first cooled to 2 K at 0 T with a cooling rate of 5 K/min. Then the magneto-transport measurement of the pristine state was carried out with magnetic field sweeping between -14 to 14 T at a sweeping rate of 100

Oe/s. Two channel fitting model ($\rho_{xy} = \frac{(n_h\mu_h^2 - n_e\mu_e^2)B + \mu_h^2\mu_e^2(n_h - n_e)B^3}{e[(n_h\mu_h + n_e\mu_e)^2 + (n_h - n_e)^2\mu_h^2\mu_e^2B^2]}$; $\rho_{xx} =$

$\frac{(n_h\mu_h + n_e\mu_e) + (n_h\mu_h\mu_e^2 + n_e\mu_e\mu_h^2)B^2}{e[(n_h\mu_h + n_e\mu_e)^2 + (n_h - n_e)^2\mu_h^2\mu_e^2B^2]}$) was applied to fit the magnetic field dependent R_{xx} and R_{xy} to

extract out the mobility (μ) and carrier density (n) of electron (e) and hole (h)¹⁷.

In situ Magneto-Transport Measurement

In situ Hall transport measurements were carried out using the DynaCool PPMS system. After the assembly of the polymer cell and wire bonding between the gold pads of the PPMS puck and the copper foil of the polymer cell, the puck was quickly transferred into the chamber of the PPMS system. Intercalation was carried out at 300 K and 3 T, and R_{xx} and R_{xy} were recorded

during the intercalation. The carrier density was determined by equations $n_H = B / (eR_{xy})$, $e =$

$1.602 \times 10^{-19} C$ ²¹. The correction of R_{xy} is obtained by subtracting the contribution of R_{xx} from

raw R_{xy} using the equation $R_{xy,corrected,3T} = R_{xy,raw,3T} - \alpha \cdot R_{xx,3T}$, where α is a geometric

factor determined by the ratio of raw R_{xy} over R_{xx} at zero field using $\alpha = R_{xy,0T} / R_{xx,0T}$.

Temperature-dependent resistance measurements were carried out by first freezing the electrochemical intercalation through a rapid cooling to 200 K at a rate of 10 K/min, at which

point the intercalation current running through the cell gradually goes to zero. Then the system was gradually cooled to 150 K at a rate of 2 K/min.

Post-mortem characterizations

Intercalation devices were disassembled by physically removing the liquid or polymer electrolyte by a razor blade. Then the device was immersed in isopropanol to further remove the residual electrolyte. The cleaned device was characterized by Raman spectroscopy (Horiba LabRAM HR Evolution Spectrometer; 633 nm) and SEM (Helios G4 FIB-SEM) with a stage tilting angle of 50° at a voltage of 5 kV and a current of 25 pA.

Ab initio Calculations

Density functional theory (DFT) calculations were carried out in a plane-wave basis set within the Projector Augmented Wave (PAW) approach^{22, 23} as implemented in the Quantum Espresso software package²⁴. The exchange-correlation was treated at the Generalized Gradient Approximation (GGA) level of Perdew, Burke, and Ernzerhof (PBE)²⁵. The van der Waals interactions were accounted for using Grimme's D3 correction with Becke-Johnson damping²⁶. A kinetic energy cut-off of 1040 eV was used for the expansion of the plane-wave basis in all the calculations, and the Brillouin zone was sampled using Gamma-centered Monkhorst-Pack²⁷ k-point meshes of 32×16×8 and 16×8×8 for the T_d (12 atoms) and T_d' (24 atoms) unit cells respectively. The unit cells were relaxed until the total energy and the force on each atom converged to within 0.02 meV/atom and 0.03 eV/Å respectively. The lithiated T_d phase was relaxed with the volume fixed to that of the pristine T_d to prevent a doping-induced phase transition. Spin-orbit coupling with non-collinear magnetization was used for all the band

structure calculations. Phonopy²⁸ was used for the calculation of phonon bands, with supercell sizes of $2 \times 2 \times 2$ and $2 \times 2 \times 1$ for T_d - and T_d' - WTe_2 phases, and q-meshes of $8 \times 4 \times 2$ and $4 \times 4 \times 4$ were used respectively. For implicitly doped T_d , a $2 \times 2 \times 1$ supercell with a q-mesh of $4 \times 4 \times 4$ was used.

References

1. Fatemi, V.; Wu, S.; Cao, Y.; Bretheau, L.; Gibson, Q. D.; Watanabe, K.; Taniguchi, T.; Cava, R. J.; Jarillo-Herrero, P., Electrically tunable low-density superconductivity in a monolayer topological insulator. *Science* **2018**, *362* (6417), 926.
2. Sajadi, E.; Palomaki, T.; Fei, Z.; Zhao, W.; Bement, P.; Olsen, C.; Luescher, S.; Xu, X.; Folk, J. A.; Cobden, D. H., Gate-induced superconductivity in a monolayer topological insulator. *Science* **2018**, *362* (6417), 922.
3. Tang, S.; Zhang, C.; Wong, D.; Pedramrazi, Z.; Tsai, H.-Z.; Jia, C.; Moritz, B.; Claassen, M.; Ryu, H.; Kahn, S.; Jiang, J.; Yan, H.; Hashimoto, M.; Lu, D.; Moore, R. G.; Hwang, C.-C.; Hwang, C.; Hussain, Z.; Chen, Y.; Ugeda, M. M.; Liu, Z.; Xie, X.; Devereaux, T. P.; Crommie, M. F.; Mo, S.-K.; Shen, Z.-X., Quantum spin Hall state in monolayer $1T'$ - WTe_2 . *Nature Physics* **2017**, *13* (7), 683-687.
4. Ono, M.; Noji, T.; Harada, M.; Sato, K.; Kawamata, T.; Kato, M., New Lithium- and Ethylenediamine-Intercalated Superconductors $Li_x(C_2H_8N_2)_yWTe_2$. *Journal of the Physical Society of Japan* **2020**, *90* (1), 014706.
5. Zhu, L.; Li, Q.-Y.; Lv, Y.-Y.; Li, S.; Zhu, X.-Y.; Jia, Z.-Y.; Chen, Y. B.; Wen, J.; Li, S.-C., Superconductivity in Potassium-Intercalated T_d - WTe_2 . *Nano Letters* **2018**, *18* (10), 6585-6590.
6. Nayak, A. K.; Steinbok, A.; Roet, Y.; Koo, J.; Margalit, G.; Feldman, I.; Almoalem, A.; Kanigel, A.; Fiete, G. A.; Yan, B.; Oreg, Y.; Avraham, N.; Beidenkopf, H., Evidence of topological boundary modes with topological nodal-point superconductivity. *Nature Physics* **2021**.
7. Sipos, B.; Kusmartseva, A. F.; Akrap, A.; Berger, H.; Forró, L.; Tutiš, E., From Mott state to superconductivity in $1T$ - TaS_2 . *Nature Materials* **2008**, *7* (12), 960-965.
8. Yu, Y.; Yang, F.; Lu, X. F.; Yan, Y. J.; Cho, Y.-H.; Ma, L.; Niu, X.; Kim, S.; Son, Y.-W.; Feng, D.; Li, S.; Cheong, S.-W.; Chen, X. H.; Zhang, Y., Gate-tunable phase transitions in thin flakes of $1T$ - TaS_2 . *Nature Nanotechnology* **2015**, *10* (3), 270-276.
9. Ye, J. T.; Zhang, Y. J.; Akashi, R.; Bahramy, M. S.; Arita, R.; Iwasa, Y., Superconducting Dome in a Gate-Tuned Band Insulator. *Science* **2012**, *338* (6111), 1193.
10. Lee, J.-H.; Son, Y.-W., Gate-tunable superconductivity and charge-density wave in monolayer $1T'$ - $MoTe_2$ and $1T'$ - WTe_2 . *Physical Chemistry Chemical Physics* **2021**, *23* (32), 17279-17286.
11. Yang, W.; Mo, C.-J.; Fu, S.-B.; Yang, Y.; Zheng, F.-W.; Wang, X.-H.; Liu, Y.-A.; Hao, N.; Zhang, P., Soft-Mode-Phonon-Mediated Unconventional Superconductivity in Monolayer $1T'$ - WTe_2 . *Physical Review Letters* **2020**, *125* (23), 237006.
12. Marini, G.; Calandra, M., Light-tunable charge density wave orders in $MoTe_2$ and WTe_2 single layers. *arXiv preprint arXiv:2111.11920* **2021**.

13. Muscher, P. K.; Rehn, D. A.; Sood, A.; Lim, K.; Luo, D.; Shen, X.; Zajac, M.; Lu, F.; Mehta, A.; Li, Y.; Wang, X.; Reed, E. J.; Chueh, W. C.; Lindenberg, A. M., Highly Efficient Uniaxial In-Plane Stretching of a 2D Material via Ion Insertion. *Advanced Materials* **2021**, *33*, 2101875.
14. Kim, M.; Han, S.; Kim, J. H.; Lee, J.-U.; Lee, Z.; Cheong, H., Determination of the thickness and orientation of few-layer tungsten ditelluride using polarized Raman spectroscopy. *2D Materials* **2016**, *3* (3), 034004.
15. Eda, G.; Yamaguchi, H.; Voiry, D.; Fujita, T.; Chen, M.; Chhowalla, M., Photoluminescence from Chemically Exfoliated MoS₂. *Nano Letters* **2011**, *11* (12), 5111-5116.
16. Ali, M. N.; Xiong, J.; Flynn, S.; Tao, J.; Gibson, Q. D.; Schoop, L. M.; Liang, T.; Haldolaarachchige, N.; Hirschberger, M.; Ong, N. P.; Cava, R. J., Large, non-saturating magnetoresistance in WTe₂. *Nature* **2014**, *514* (7521), 205-208.
17. Woods, J. M.; Shen, J.; Kumaravadeivel, P.; Pang, Y.; Xie, Y.; Pan, G. A.; Li, M.; Altman, E. I.; Lu, L.; Cha, J. J., Suppression of Magnetoresistance in Thin WTe₂ Flakes by Surface Oxidation. *ACS Applied Materials & Interfaces* **2017**, *9* (27), 23175-23180.
18. Tang, W.; Sanville, E.; Henkelman, G., A grid-based Bader analysis algorithm without lattice bias. *Journal of Physics: Condensed Matter* **2009**, *21* (8), 084204.
19. Yazdani, S.; Pondick, J. V.; Kumar, A.; Yarali, M.; Woods, J. M.; Hynek, D. J.; Qiu, D. Y.; Cha, J. J., Heterointerface Effects on Lithium-Induced Phase Transitions in Intercalated MoS₂. *ACS Applied Materials & Interfaces* **2021**, *13* (8), 10603-10611.
20. Pondick, J. V.; Kumar, A.; Wang, M.; Yazdani, S.; Woods, J. M.; Qiu, D. Y.; Cha, J. J., Heterointerface Control over Lithium-Induced Phase Transitions in MoS₂ Nanosheets: Implications for Nanoscaled Energy Materials. *ACS Applied Nano Materials* **2021**.
21. Bediako, D. K.; Rezaee, M.; Yoo, H.; Larson, D. T.; Zhao, S. Y. F.; Taniguchi, T.; Watanabe, K.; Brower-Thomas, T. L.; Kaxiras, E.; Kim, P., Heterointerface effects in the electrointercalation of van der Waals heterostructures. *Nature* **2018**, *558* (7710), 425-429.
22. Blöchl, P. E., Projector augmented-wave method. *Physical Review B* **1994**, *50* (24), 17953-17979.
23. Dal Corso, A., Pseudopotentials periodic table: From H to Pu. *Computational Materials Science* **2014**, *95*, 337-350.
24. Giannozzi, P.; Baroni, S.; Bonini, N.; Calandra, M.; Car, R.; Cavazzoni, C.; Ceresoli, D.; Chiarotti, G. L.; Cococcioni, M.; Dabo, I., QUANTUM ESPRESSO: a modular and open-source software project for quantum simulations of materials. *Journal of physics: Condensed matter* **2009**, *21* (39), 395502.
25. Perdew, J. P.; Burke, K.; Ernzerhof, M., Generalized gradient approximation made simple. *Physical review letters* **1996**, *77* (18), 3865.
26. Becke, A. D.; Johnson, E. R., A density-functional model of the dispersion interaction. *The Journal of chemical physics* **2005**, *123* (15), 154101.
27. Monkhorst, H. J.; Pack, J. D., Special points for Brillouin-zone integrations. *Physical Review B* **1976**, *13* (12), 5188-5192.
28. Togo, A.; Tanaka, I., First principles phonon calculations in materials science. *Scripta Materialia* **2015**, *108*, 1-5.
29. Mehl, M. J.; Hicks, D.; Toher, C.; Levy, O.; Hanson, R. M.; Hart, G.; Curtarolo, S., The AFLOW library of crystallographic prototypes: part 1. *Computational Materials Science* **2017**, *136*, S1-S828.

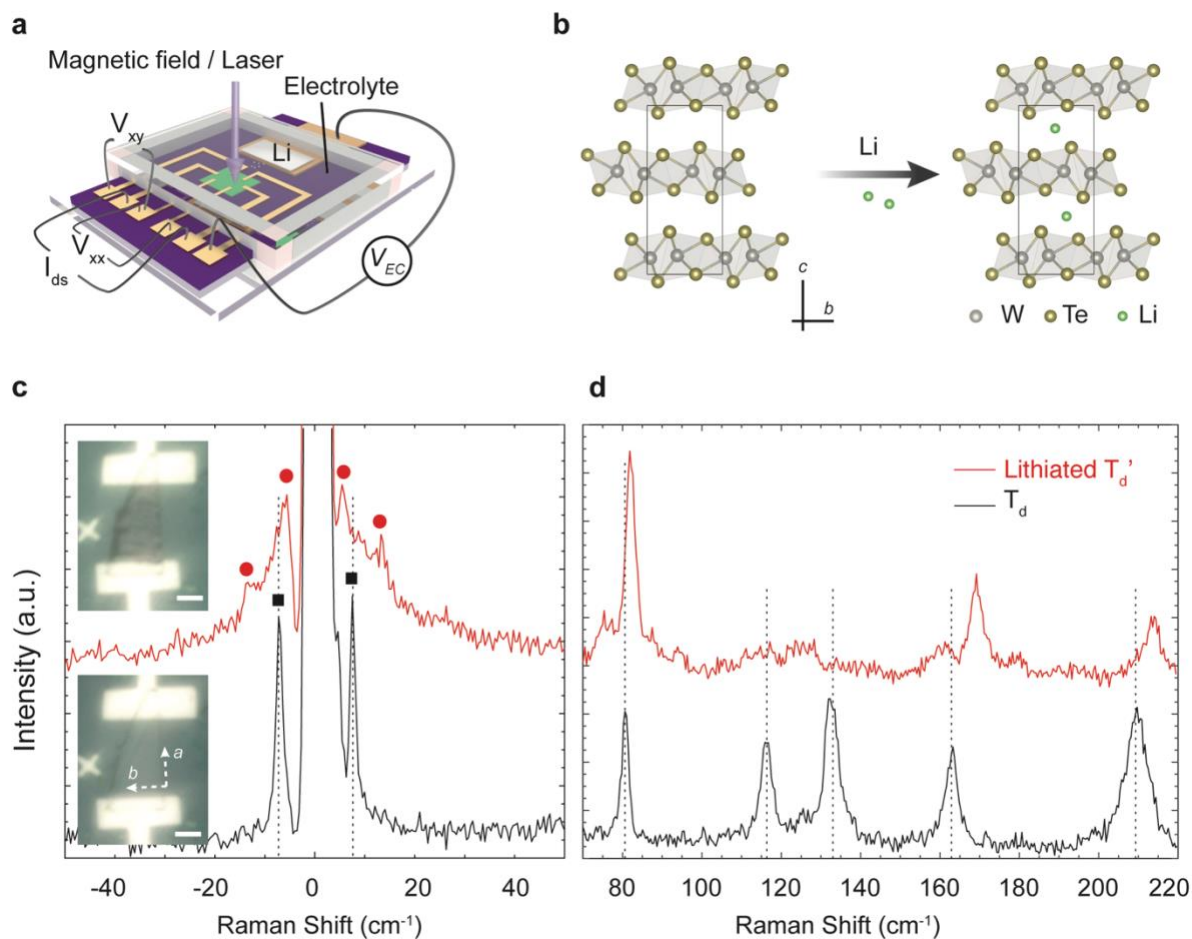


Figure 1. Phase transition in T_d -WTe₂ induced by lithium intercalation. **(a).** Schematic of a lithium-ion electrochemical cell with capabilities of *in situ* Raman and *in situ* Hall measurement. V_{EC} represents the electrochemical intercalation voltage applied between the Li (silver rectangle) and WTe₂ (green rectangle). **(b).** Side-view of lithium intercalation in the van der Waals gaps of T_d -WTe₂ (W: grey, Te: gold, Li: green). **(c-d).** Low frequency **(c)** and high frequency **(d)** Raman spectra of the T_d phase (black, bottom) and lithiated T_d' phase (red, top). Insets in **c** are the corresponding optical images of the WTe₂ device before (bottom) and after (top) the phase transition. Scale bars are 10 μ m. Red circles and black squares in **c** mark the positions of Raman active modes in T_d and the new phase, respectively. Black vertical dashed lines in **c** and **d** are visual guides for the positions of Raman modes in T_d phase.

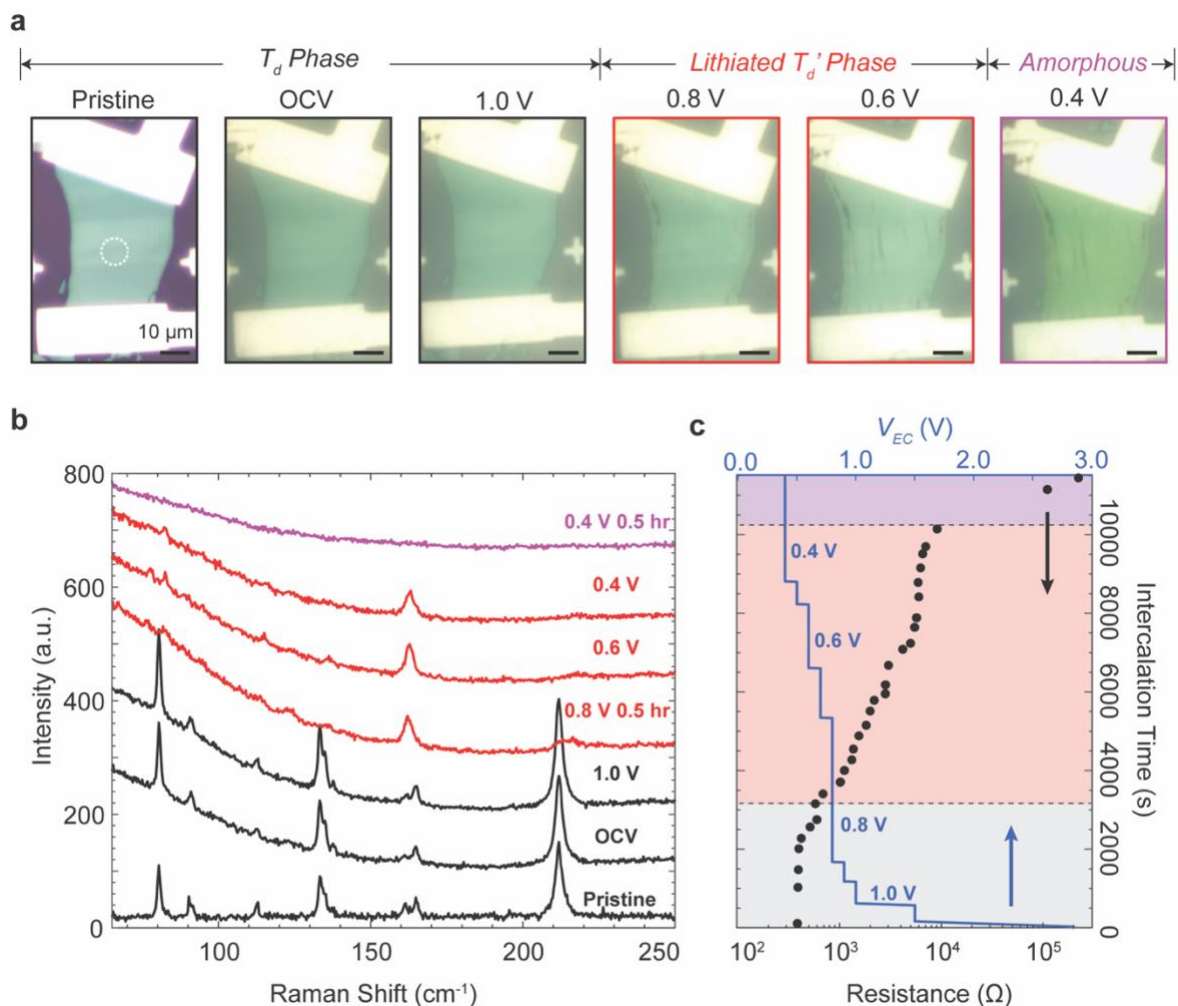


Figure 2. *In situ* optical characterization and two terminal electrical transport measurements of a WTe₂ device as a function of electrochemical intercalation voltage. **(a).** Optical images of a WTe₂ device as a function of intercalation driving voltage. According to the optical contrast, the intercalation consists of three stages: T_d phase (black framed), new phase (red framed), and amorphous state (purple framed). The white dashed circle denotes the position for *in situ* Raman data collection. **(b).** Stacking plot of high frequency Raman spectra as a function of intercalation voltage with the color scheme corresponding to the phase separation in **(a)**. The background of the Raman spectra from OCV to 0.4 V comes from the polymer electrolyte. **(c).** Simultaneous two terminal resistance (solid black circles) as function of intercalation time with the intercalation direction lined up with the Raman stacking sequence in **(b)**. The blue line is the profile of electrochemical intercalation voltage as a function of time. In line with **(a)** and **(b)**, three phases are divided and colored correspondingly.

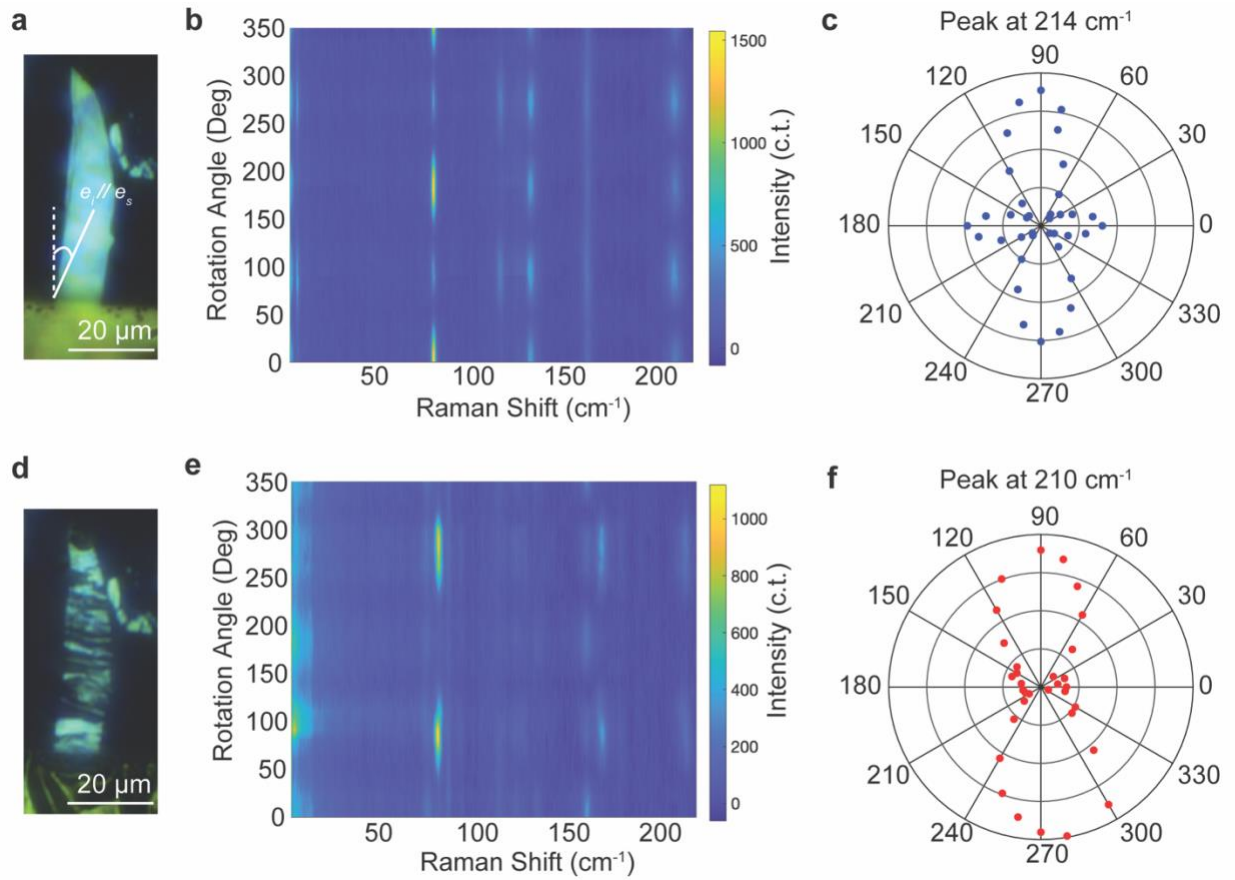


Figure 3. Angle-resolved Raman characterization of T_d (**a-c**) and lithiated T_d' - WTe_2 (**d-f**). (**a**) and (**d**) are optical images of the WTe_2 flake at pristine T_d (**a**) and lithiated T_d' (**d**) phase, respectively. The angle is defined as the angle between the vertical white dashed line and the polarization direction of the incident/scattered beam in (**a**). (**b**) and (**e**) are the angle-resolved Raman spectral maps of the T_d (**b**) and lithiated T_d' (**e**) phase, respectively. (**c**) and (**f**) are the pole graphs of the Raman peak centered around 210 cm^{-1} in T_d (**c**) and lithiated T_d' (**f**) phase, respectively.

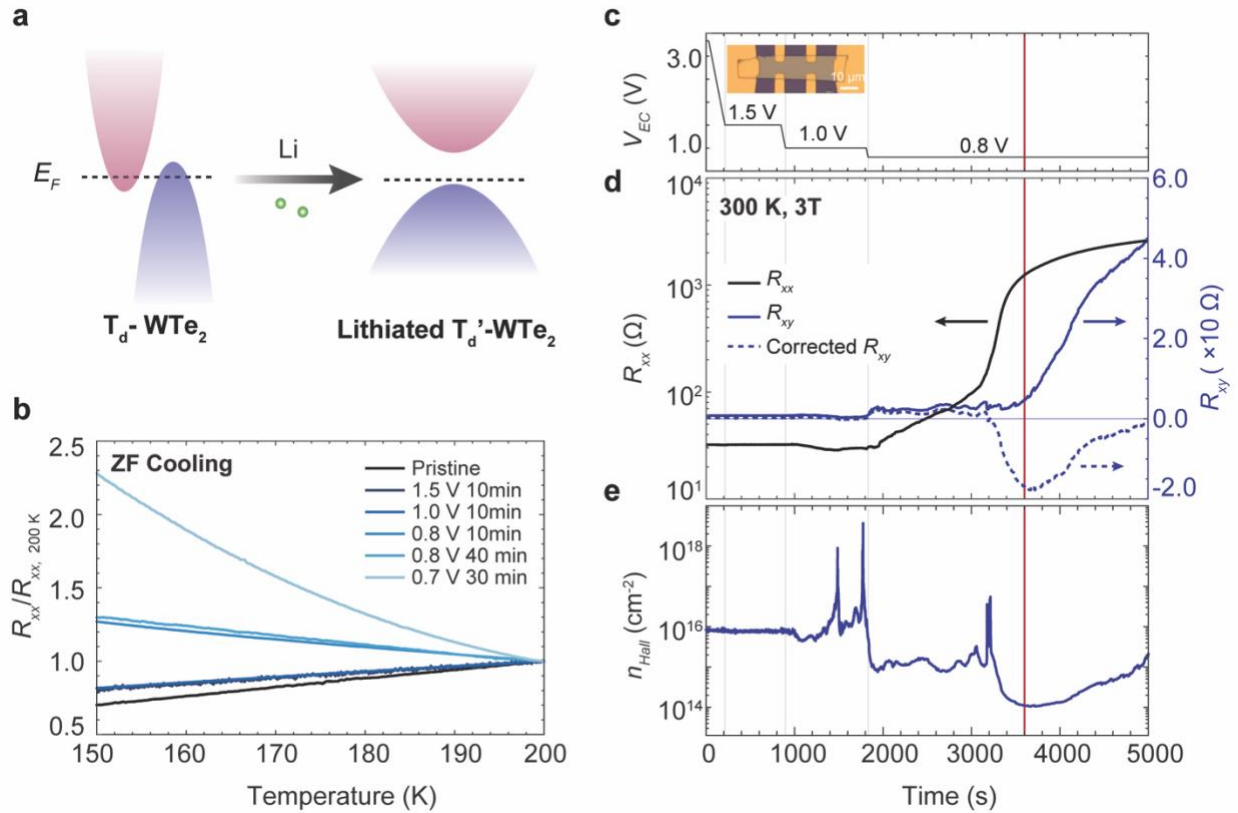


Figure 4. *In situ* Hall measurement of a WTe₂ device as a function of lithiation at 300 K. **(a)**. Schematic of electronic band structure changes during the phase transition from T_d-WTe₂ to lithiated T_d'-WTe₂. **(b)**. Zero field (ZF) cooling curves of R_{xx} at pristine state (black) and various stages of intercalation (blue). A limited temperature window from 200 K to 150 K was due to the polymer electrolyte instability below 150 K. **(c)**. Profile of electrochemical intercalation voltage as a function of intercalation time. **(d)**. Raw data of R_{xx} (black) and R_{xy} (blue), and corrected R_{xy} (blue dashed, see Methods) as a function of intercalation time at 3 T and 300 K. The grey horizontal line marks the position of zero for R_{xy} . Inset is the optical image of a WTe₂ Hall bar device. **(e)**. Carrier density determined from corrected R_{xy} as a function of intercalation time. The light grey vertical lines in (c-e) mark the time of applying each new intercalation voltage. The dark red vertical line in (c-e) denotes the time when new Raman modes emerge.

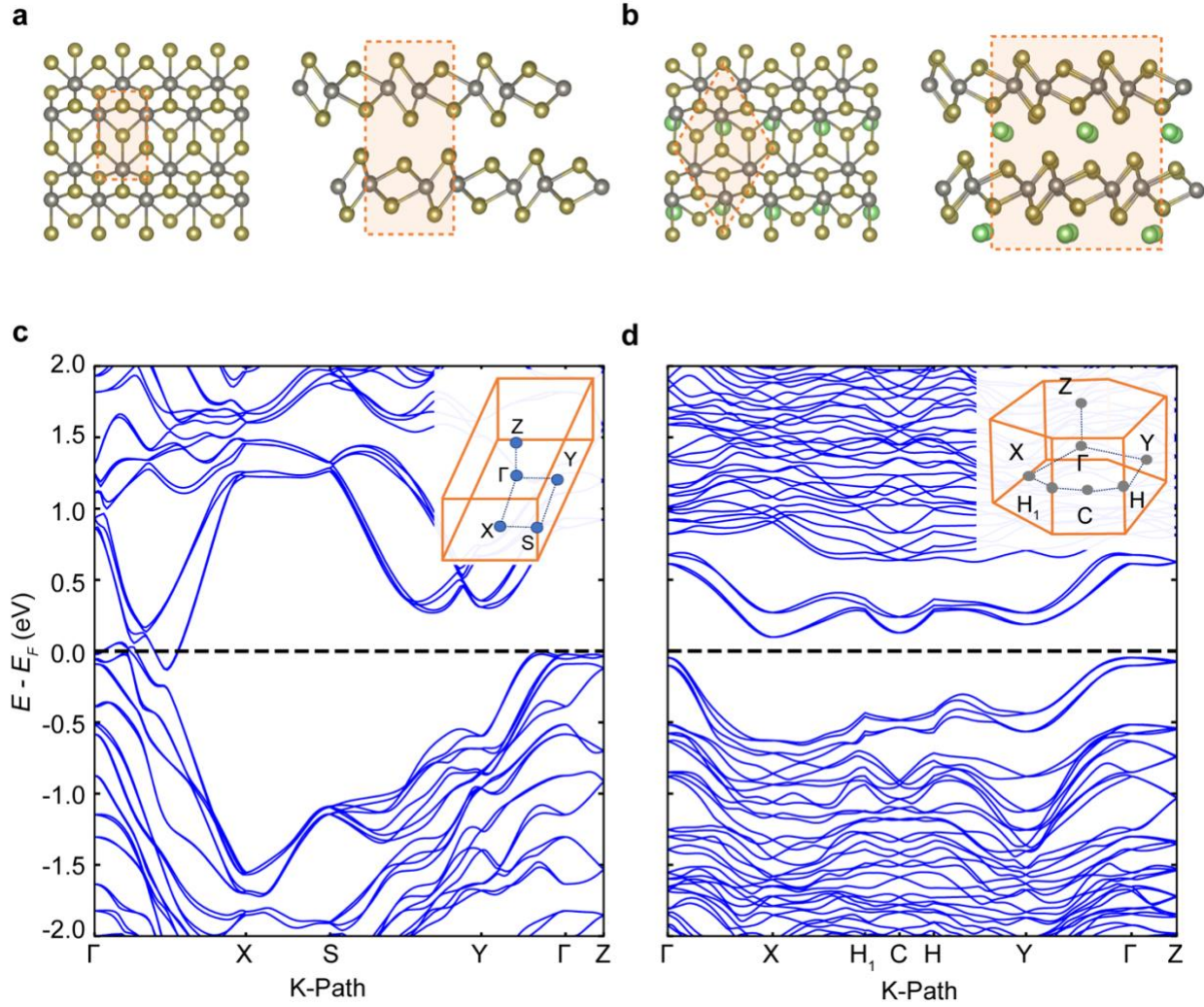


Figure 5. In-plane and cross-sectional atomic structures of T_d -WTe₂ (a) and lithiated T_d' -Li_{0.5}WTe₂ (b) with W atoms in grey, Te atoms in gold, and Li atoms in green. Unit cells are highlighted with orange dashed lines. DFT electronic band structures of (c) T_d -WTe₂ and (d) lithiated T_d' -Li_{0.5}WTe₂ along a high-symmetry K-path in Brillouin zone, as shown in the inset²⁹, reveal their semi-metallic and semiconducting nature, respectively. The horizontal black dashed line in (c) and (d) marks the Fermi level for each phase.

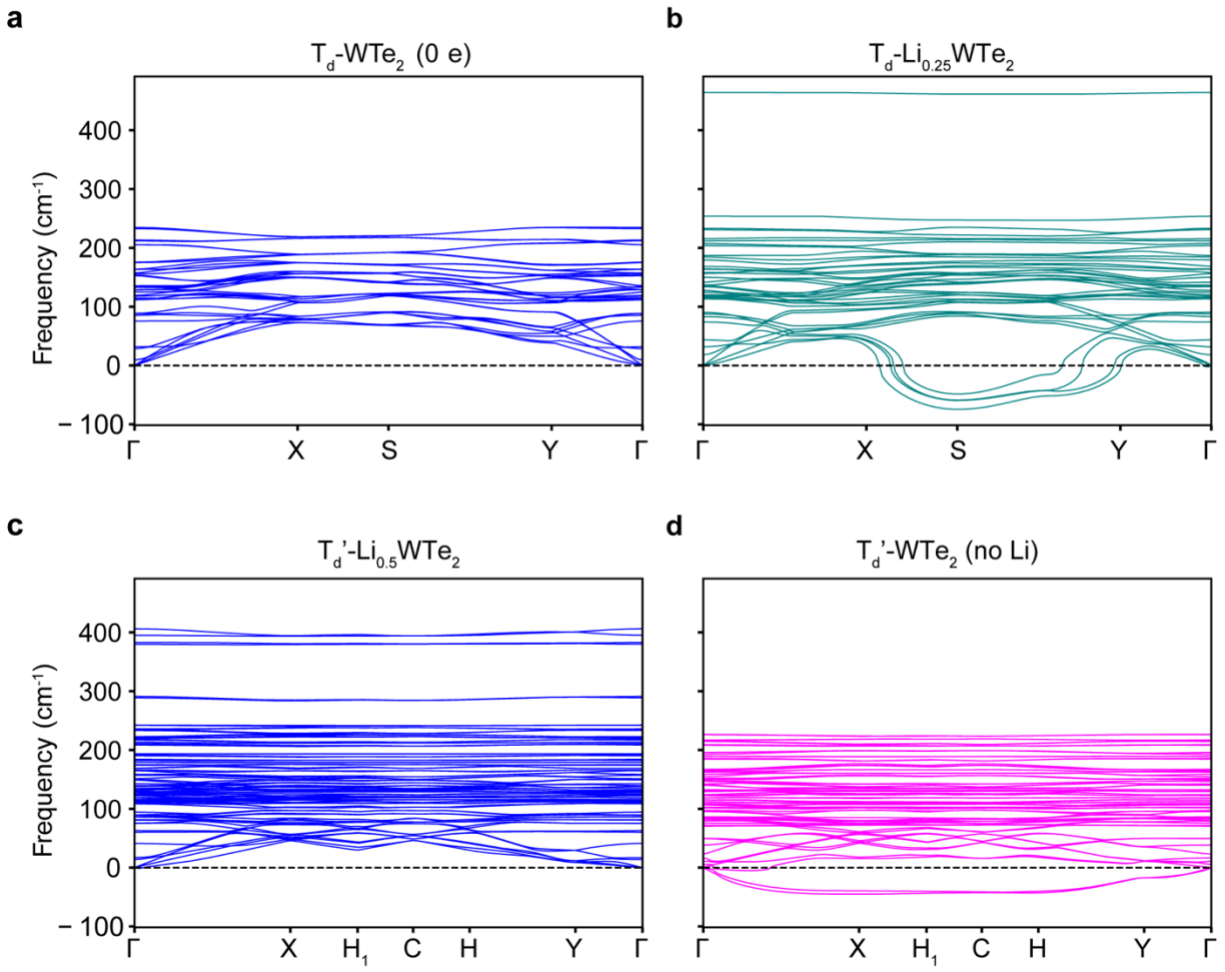


Figure 6. Phonon-dispersion of (a) T_d - WTe_2 , (b) lithiated T_d - $Li_{0.25}WTe_2$, (c) lithiated T_d' - $Li_{0.5}WTe_2$ phase, and (d) T_d' - WTe_2 without any Li atoms.